




Structural, spectral, dielectric, and magnetic properties of indium substituted $\text{Cu}_{0.5}\text{Zn}_{0.5}\text{Fe}_{2-x}\text{O}_4$ magnetic oxides

Muhammad Junaid^{1,2,*}, Muhammad Azhar Khan^{1,*} , Tahani I. Al-Muhimeed³, Abeer A. AlObaid³, Ghazanfar Nazir⁴, Thamraa Alshahrani^{5,*}, Q. Mahmood⁶, and Majid Niaz Akhtar⁷

¹Institute of Physics, The Islamia University of Bahawalpur, Bahawalpur 63100, Pakistan

²Department of Physics, The Islamia University of Bahawalpur, Rahim Yar Khan Campus, Rahim Yar Khan 64200, Pakistan

³Department of Chemistry, College of Science, King Saud University, P.O. Box 22452, Riyadh 11451, Saudi Arabia

⁴Department of Chemistry, Inha University, 100 Inharo, Incheon 22212, South Korea

⁵Department of Physics, College of Science, Princess Nourah Bint Abdulrahman University, Riyadh 11671, Saudi Arabia

⁶Basic & Applied Scientific Research Center, and Department of Physics, Imam Abdulrahman Bin Faisal University, P.O. Box 1982, Ad Dammām 31441, Saudi Arabia

⁷Department of Physics, Muhammad Nawaz Sharif University of Engineering and Technology (MNSUET), Multan 60000, Pakistan

Received: 18 April 2021

Accepted: 24 September 2021

Published online:

12 November 2021

© The Author(s), under exclusive licence to Springer Science+Business Media, LLC, part of Springer Nature 2021

ABSTRACT

The influence of indium on the properties of $\text{Cu}_{0.5}\text{Zn}_{0.5}\text{Fe}_2\text{O}_4$ nano ferrites synthesized by sol–gel auto-combustion technique was studied. X-ray diffraction (XRD) analysis demonstrated that pure and substituted ferrites possessed cubic spinel structure. The lattice parameter increases with the inclusion of In^{3+} for $x \leq 0.16$ and decreases subsequently. A linear decrease in crystallite size was found as concentration of indium increased. X-ray density, strain, and dislocation density were increased as indium content increases. Hopping lengths as well as radii of A and B sites revealed increasing behavior up to $x = 0.16$ and decreased thereafter. The spectral bands indicated the formation of spinel structure. The band positions were altered with the increase of In^{3+} contents. The inclusion of indium ions increases the value of dielectric parameters while magnetic parameters decreased. This increase in dielectric parameters and decrease in magnetization proposed that synthesized magnetic oxides may have potential in the fabrication of switching and high-frequency devices.

Address correspondence to E-mail: junaid.malik95@yahoo.com; azhar.khan@iub.edu.pk; thmalshahrani@pnu.edu.sa

1 Introduction

The researchers and scientists have great interest in spinel ferrites due to their utilization in many fields i.e., circulators, transformers core, data storage devices, switching, gas sensing, radio frequency circuits, antennas, microwave, drug delivery, and high-frequency appliances [1–4]. Spinel ferrites have interesting and excellent structural, electrical, dielectric, and magnetic properties. The characteristics of spinel ferrites depend upon many factors such as structure, crystallite size, density, synthesis method, and substitution of cations [5–9]. The cations distribution among tetrahedral and octahedral sites strongly affects the properties of synthesized ferrites. The interactions between the cations are mainly affected by magnetic properties of spinel ferrites. There are three types of super exchange interactions (A–A, B–B and A–B) present in the spinel ferrites. When A–B superexchange interaction is stronger than (A–A and B–B) then it represents a collinear spin structure. If A–A or B–B superexchange interaction is comparable with A–B exchange interaction then it leads to non-collinear spin structure [10, 11].

Copper–zinc ferrites are crystallized as spinel ferrites that exhibit ferrimagnetic and semiconducting behavior. The antiparallel spins of magnetic moment of atoms among interstitial sites give ferrimagnetic characteristics. The structural properties can be controlled by substituting various kinds of atoms having different radius, magnetization, and atomic weight in the spin–lattice [12–15]. Copper ferrites possessed an inverse spinel structure and shows ferrimagnetic at room temperature. Zinc ferrites owing normal spinel structure in bulk with $T_N = 10$ K and exhibited anti-ferromagnetic below Neel's temperature (10 K). ZnFe_2O_4 nano ferrites become paramagnetic at room temperature. Cu^{2+} ions preferentially occupied at octahedral sites while Zn^{2+} preferentially occupied on tetrahedral sites. Fe^{3+} cations are disturbed among tetrahedral and octahedral sites [16, 17]. Variation in the magnetic properties of Cu–Zn nano ferrites is attributed to the distribution of iron ions on two sites with tetrahedral and octahedral coordination of oxygen ions. If divalent cations go to tetrahedral voids only while trivalent cations occupied octahedral voids, then structure was said to be normal spinel. Special attention is required to understand the structural and magnetic properties of copper–zinc ferrites.

Polymer composite is emerging field of materials and has great interest due to wide range of applications. The polymer composites are used in many fields such as light emitting diode, transistors, radar applications, sensors and materials batteries. From different types of composites, solid polymers are important due to variety of application in different fields such as solar cells, electro chromic windows, fuel cells and energy storage devices. The important parameter which controls the various properties of combined matrix of composites is degree of miscibility [18–20].

Novel synthesis techniques are applied to attain definite structural and magnetic properties [21–23]. The various methods are used to synthesis spinel ferrites, but some most common methods are hydrothermal, co-precipitation, solid-state reaction, sol–gel, and micro-emulsion route [11, 24–27]. Sol–gel auto-combustion route offers various advantages over other methods including definite particle size, lab friendly, cost-effective, and processed at low temperature with the best homogeneity. Single-phase Cu–Zn nano ferrites can be obtained by sol–gel auto-combustion method [28]. The variation in structural and magnetic parameters of copper–zinc ferrites is observed by the substitution of indium ions. There is no report on indium incorporated copper–zinc ferrites in our best knowledge. The researchers prepared spinel ferrites at high temperature and reported the value of crystallite size, dielectric constant and dielectric losses are very high. We synthesized In^{3+} incorporated Cu–Zn ferrites at low temperature 500 °C. The value of crystallite size remains in the range 9.37–14.76 nm. The value of dielectric constant and dielectric losses is very small as compared to reported literature [29–31].

The objective of this research work is to explore the influence of indium on structural, spectral, dielectric and magnetic properties of $\text{Cu}_{0.5}\text{Zn}_{0.5}\text{In}_x\text{Fe}_{2-x}\text{O}_4$ ferrites. These ferrites are synthesized by novel synthesis route (sol–gel auto-combustion). Here we reported our results on structural, spectral bands/bond length, magnetic and dielectric properties which are characterized by XRD, FTIR, VSM, and dielectric.

2 Experimental procedure

The indium incorporated Cu–Zn nanocrystalline ferrites were synthesized by sol–gel auto-combustion route. The analytical grades copper nitrate, zinc nitrate, iron nitrate, indium nitrate, and citric acid were utilized without any purification in 1:1 stoichiometric ratio of metals nitrate to citric acid. All the reagents were weighed and dissolved in deionized water. Furthermore, all solutions were heated at 45 °C with continuous stirring. The pH value was maintained by adding ammonia solution ~ 7 . Moreover, all the solution mixture was continuously stirred as well as heating at the temperature 90 °C. The water molecules were evaporated, and the formation of sol was developed. The gel was obtained by stirring the solutions for 3 h at 90 °C. The gel was self-ignited and burned entirely by auto-combustion method to make fluffy powder. Finally, the prepared powder was sintered at 500 °C for 4.30 h to remove organic matter and to form spinel phase. Polyvinyl alcohol (PVA) 5% was added to calcined powder as binder. The powder was pressed by hydraulic pressure to obtain a pellet of diameter 7 mm. The pellet was heated at 160 °C for 2 h. D8 Advance Bruker, Cu $K\alpha$ was used for the crystal structure of sintered powder. FTIR spectra were recorded by Nicolet TM 5700 spectrophotometer. The dielectric property of synthesized ferrites was carried out by Keithley LCR meter model-197. $M-H$ loops were obtained using vibrating sample magnetometer (VSM) Lakeshore model-7300.

3 Results and discussion

3.1 Thermal analysis

The phase transformation of copper–zinc ferrite sample was studied by thermal analysis. Thermal analysis of pure ferrite depicted in Fig. 1. The weight loss in TGA and DTA curves occurred in four successive steps. There are four peaks observed in TGA and DTA curves due to disintegration of residual components. First weight loss of $\sim 2\%$ was observed due to water evaporation. Second weight loss $\sim 3\%$ and third weight loss $\sim 2\%$ was observed due to disintegration of residual components. After that very small weight loss was observed that indicated the spinel phase formation. The first exothermic peak

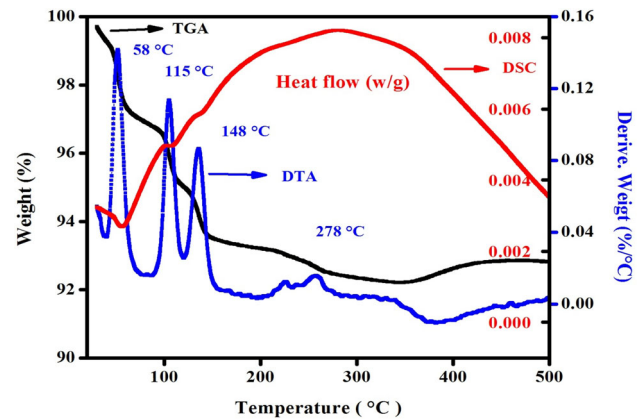


Fig. 1 Thermal analysis of $\text{Cu}_{0.5}\text{Zn}_{0.5}\text{Fe}_2\text{O}_4$ ferrites

which appeared below 100 °C was due to moisture or water trapped in the pores of prepared ferrite. The exothermic peaks that occurred at 115 °C and 148 °C were due to decomposition of metal nitrates. The overall weight loss observed in the thermal analysis was 8%. TGA curve shows the spinel phase formation occurred after 400 °C. Three exothermic peaks appeared in DSC curve are associated with DTA peaks. DSC analysis provides information about reactions i.e., exothermic or endothermic. DSC curve revealed that decomposition process is strongly exothermic. The sintering temperature for indium substituted copper ferrites was estimated from TGA curve. The sintering of synthesized nano ferrites was carried out at 500 °C for 430 h [32, 33].

3.2 Structural analysis

X-ray diffraction (XRD) patterns of $\text{Cu}_{0.5}\text{Zn}_{0.5}\text{In}_x\text{Fe}_{2-x}\text{O}_4$ nanocrystalline ferrites are displayed in Fig. 2. XRD pattern of pure sample exhibited only spinel phase and no additional phase appeared during sintering process. All the peaks (111), (220), (311), (400), (422), (511) and (440) were well indexed and matched with the ICDD card No. 01-089-7409. All the samples possessed spinel structure having cubic symmetry with space group $Fd\bar{3}m$ [34]. The various parameters such as crystallites size, lattice constant, and cell volume are calculated from XRD data and listed in Table 1. Lattice parameter increases with the substitution of In^{3+} up to $x = 0.16$ and decreases afterward. The variation occurred in the lattice parameter is ascribed by ionic radii. The increase in lattice parameter is due to incorporation of higher ionic radius In^{3+} ions instead of Fe^{3+} ions and

Fig. 2 XRD patterns of Cu–Zn–In–Fe–O system

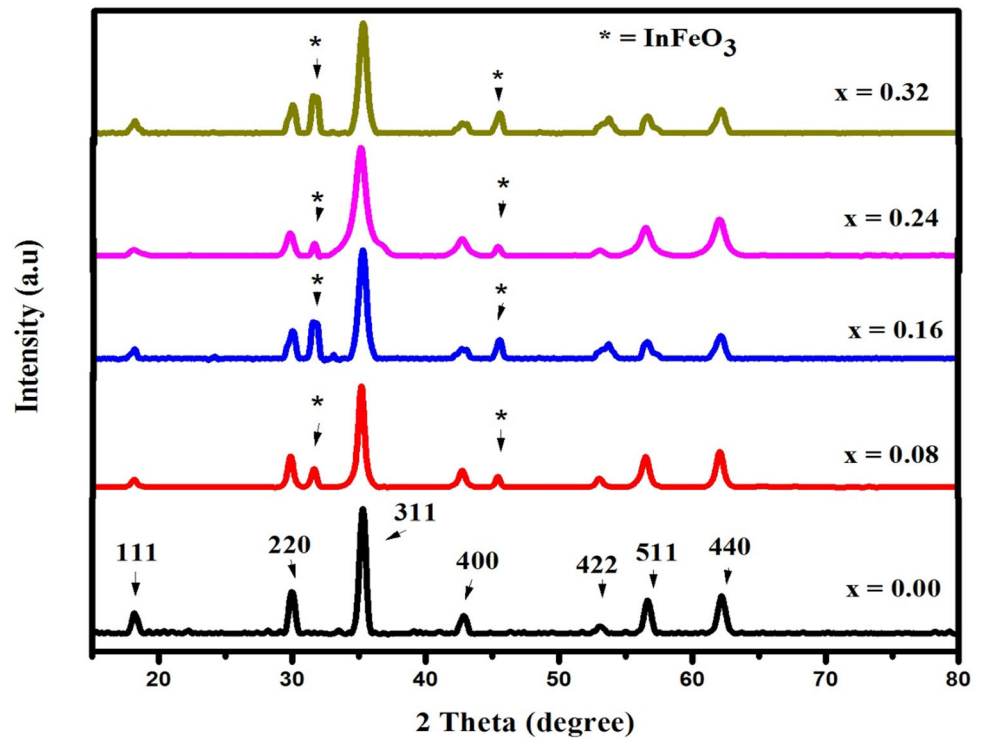


Table 1 The structural parameters of In–Cu–Zn–Fe–O ferrites

Concentration, x	Lattice constant, a (Å)	Crystallite size, D (nm)	Cell volume, V (Å ³)	Bulk density, ρ_b (g/cm ³)	X-ray density, ρ_x (g/cm ³)
0.00	8.4446	14.76	602.19	2.99	5.30
0.08	8.4460	14.57	602.49	3.06	5.40
0.16	8.4588	13.19	605.23	2.63	5.48
0.24	8.4579	11.48	605.04	3.05	5.56
0.32	8.4554	9.37	604.51	2.73	5.69

decrease due to the presence of an additional phase [35].

The crystallite size (D) determined from Scherrer's relation using (311) Bragg's reflection peak decreases monotonically with the increase of indium contents and shown in Fig. 3. The value of ' D ' remains in the range of 9.37–14.76 nm. The decrease in ' D ' produces an increase in strain. When higher ionic radii In^{3+} are replaced with Fe^{3+} ions, the lattice strain is produced because larger ions enter the spinel lattice of copper-zinc ferrites produced internal stress [36]. It was observed that most intense peak (311) was shifted towards a lower angle which may be due to an increase in cell volume and lattice constant. When indium concentration increases, In^{3+} ions isolate from the crystal structure of $\text{Cu}_{0.5}\text{Zn}_{0.5}\text{Fe}_2\text{O}_4$ and

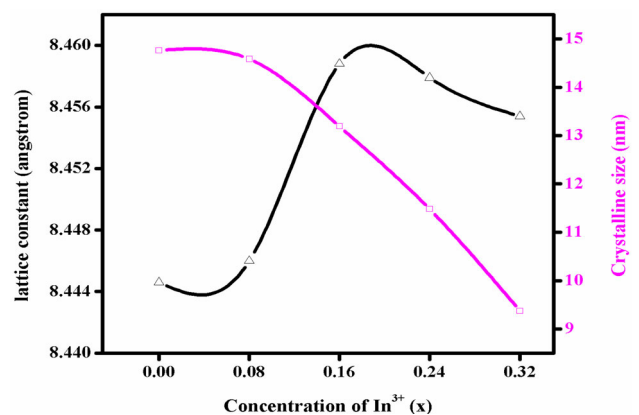


Fig. 3 Lattice parameter and crystallite size versus In^{3+} contents

form InFeO_3 phase. The extra phase appeared in XRD patterns was InFeO_3 and matched with the ICDD no.

01-085-2306. The impurity phase appeared in XRD patterns were indicated by (*). The cell volume increases with the inclusion of In^{3+} ions and decrease for higher concentration. Initially the indium ions enter into the lattice of Cu–Zn and isolated from the lattice for higher x . The increase in cell volume due to expand of volume and decrease in cell volume ascribed due to contract of cell volume.

Rietveld refinement of In^{3+} substituted Cu–Zn ferrites was carried out by MAUD (materials analysis using diffraction) software. Figure 4 reveals Rietveld refined XRD patterns of all samples. It was observed that experimental data and standard data are matched. The pure sample exhibited single phase spinel structure while indium substituted samples showed some extra peaks of InFeO_3 which elaborated by (*). The refined parameters of XRD patterns for all samples are listed in Table 2. R -factor described the quality and refinement of prepared samples. The quality of synthesized samples can be obtained by determining R_{wp} , R_b , R_{wpb} , R_{exp} and GOF. GOF (goodness of fit) is simply the ratio of R_{wp} and R_{exp} . The refinement quality was considered reliable only when $1 \leq \chi^2 < 2$. The best refined structure is demonstrated by sig value close to one. The value of

GOF is in the range of 1–2 which shows the reliability of present study. The values of lattice parameter and cell volume calculated from the refined patterns are close to experimental one and listed in Table 2 [37–41].

X-ray density increases with the increase of indium content and displayed in Fig. 5. The increase in X-ray density is due to the denser ions replaced with lighter ions. It was expected that theoretical density will increase with the substitution of indium ions due to high molecular weight and density of In^{3+} ions. The bulk density is calculated by following relation $\rho_b = m/\pi r^2 h$. The bulk density has nonlinear behavior. Overall bulk density is increased with the increase of dopant concentration. The value of bulk density is smaller than X-ray density due to occurrence of pores during sintering process. Dislocation density, strain tetrahedral and octahedral radii, and hopping length were calculated from XRD data. Strain is calculated from William–Hall plots and listed in Table 3. It can be seen that strain increases with the substitution of In^{3+} ions. The increase in strain may be due to increase of internal stress of large ionic radii incorporation. It may be due to presence of secondary phases in the crystal structure. Dislocation density

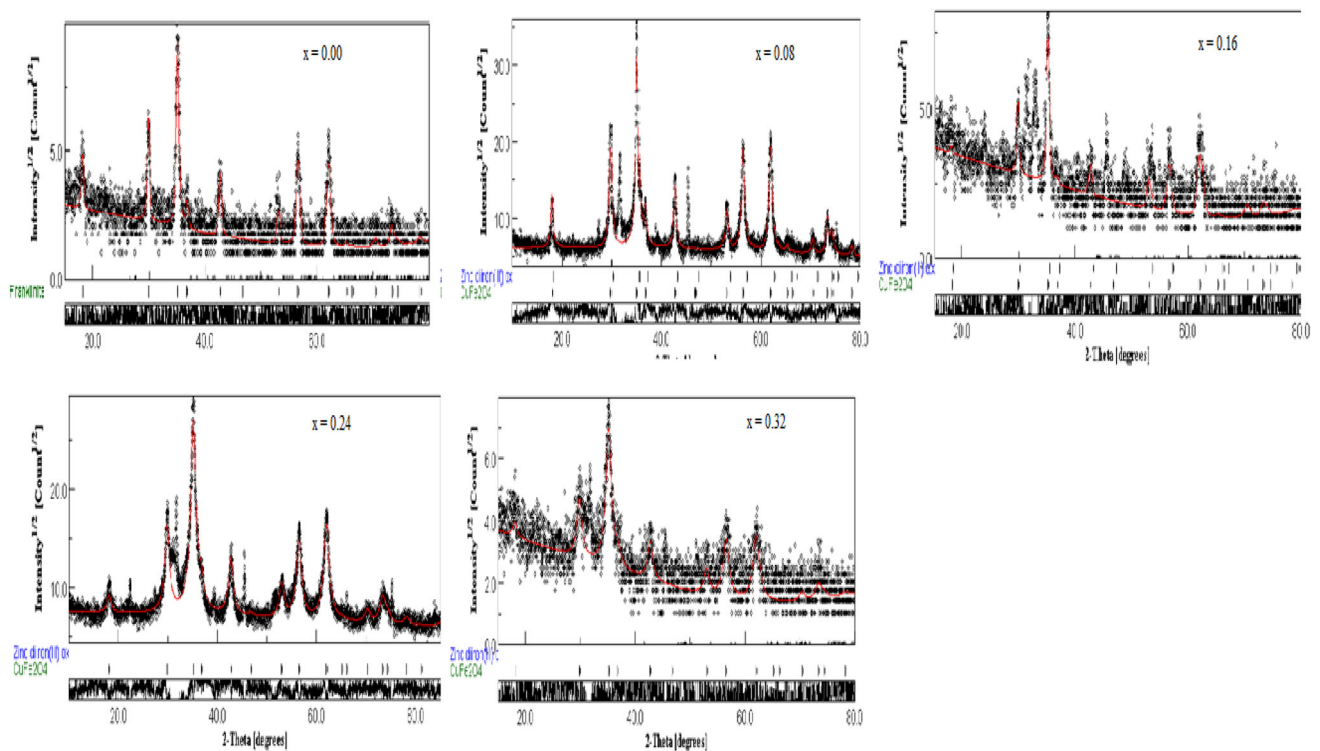
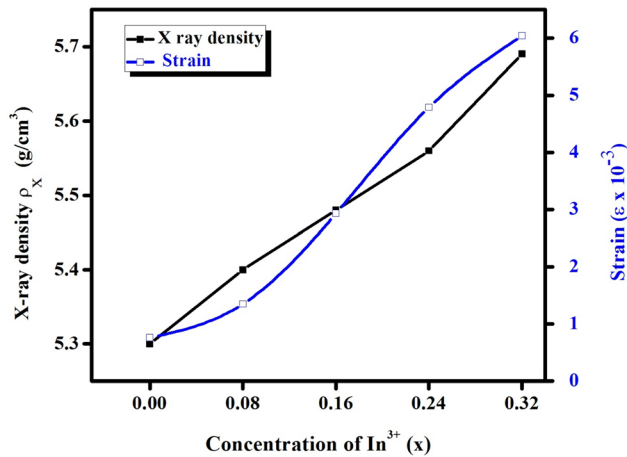


Fig. 4 XRD patterns of Cu–Zn–In–Fe–O system

Table 2 Rietveld refined parameters of Cu–Zn–In–Fe–O system

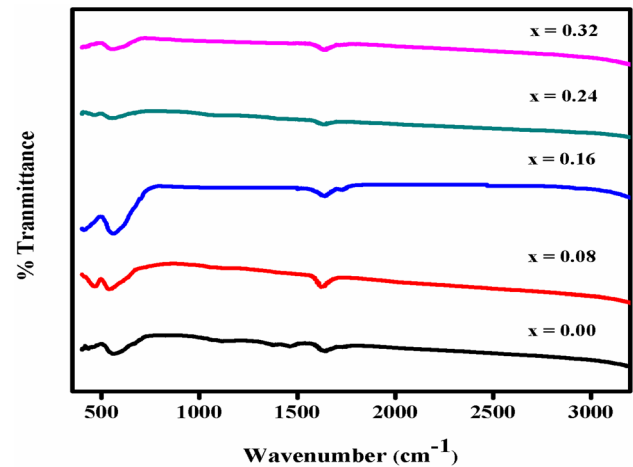
Samples, x	Lattice parameter	Cell volume	R_{wp} (%)	R_b (%)	R_{wpnb}	R_{exp} (%)	Significance (GOF)	Phase
0.00	8.4488	603.09	40.71	32.75	64.44	40.70	1.00	Cubic
0.08	8.4557	604.57	24.63	17.88	40.01	12.38	1.98	Cubic
0.16	8.4462	602.53	45.03	36.11	82.15	36.03	1.25	Cubic
0.24	8.4628	606.09	19.68	14.52	35.63	10.90	1.81	Cubic
0.32	8.4576	604.98	38.66	29.99	69.17	34.79	1.11	Cubic

**Fig. 5** X-ray density and strain versus In^{3+} contents

has direct relation with strain an inverse relation with crystallite size. The behavior of dislocation density is explained on the basis of crystallite size and strain. The value of dislocation density increases due to rise in strain. The behavior of dislocation density is in accordance with the D and ε . The hopping length of tetrahedral sites (L_A) and octahedral sites (L_B) is determined from structural data. The L_A is the distance between magnetic ions at tetrahedral sites and L_B is the distance between ions at octahedral sites. The hopping length improved as the percentage of indium increases and reduced for higher x . An increase in hopping length indicated that charge carriers required more energy for the hopping between one cation sites to another. Sometimes hopping was also called the distance between centers of adjacent ions. The behavior of these radii is the same as of lattice constant [42, 43].

3.3 Spectral analysis

The structural and chemical changes occurred during combustion were investigated by spectroscopic

**Fig. 6** FTIR spectra of In^{3+} inclusion Cu–Zn ferrites

analysis. The combustion reaction phenomenon can be studied with the help of infrared analysis. Figure 6 shows the infrared spectra of indium substituted copper–zinc ferrites. The band ν_1 ($539\text{--}560\text{ cm}^{-1}$) and ν_2 ($454\text{--}464\text{ cm}^{-1}$) correspond to cubic spinel structure [27, 44, 45]. The band ν_1 occurred due to stretching vibration of metal–oxygen ($M_{\text{tetra-O}}$) at tetrahedral sites while octahedral band ν_2 in the FTIR spectra was attributed to vibration of $M_{\text{octa-O}}$ at octahedral sites. FTIR analysis also confirmed the spinel structure of synthesized ferrites [46]. The high-frequency band tilted towards low frequency with the substitution of In^{3+} ions. There is an inverse relationship between both bands. The shifting of bands depends upon cations mass, lattice parameter, and bonding of cations with oxygen. The shifting of bands towards lower frequency may be due to the decrease in metal stretching vibrations energies. As a result, covalent bonding between metal–oxygen decreased.

The value of absorption band ν_1 was high as compared to ν_2 due to variation in bond length [47]. The bond length exhibited an increasing behavior for $x \leq 0.16$ and decrease for higher x . The peak

Table 3 The various structural parameters of indium incorporated copper–zinc ferrites

Concentration, x	Strain (β)	Strain W–H (plot) $\varepsilon \times 10^{-3}$	Dislocation density, δ	L_A (Å)	L_B (Å)	R_t (Å)	R_o (Å)
0.00	0.113	0.76	0.013	2.9856	3.6566	0.4483	0.7311
0.08	0.115	1.35	0.014	2.9861	3.6557	0.4486	0.7315
0.16	0.127	2.93	0.017	2.9906	3.6627	0.4513	0.7347
0.24	0.146	4.79	0.022	2.9903	3.6623	0.4511	0.7344
0.32	0.179	6.04	0.033	2.9894	3.6612	0.4506	0.7338

Table 4 The spectral parameters of In^{3+} substituted Cu–Zn ferrites

Concentration, x	Molecular weight (g/mol)	ν_1 (cm^{-1})	ν_2 (cm^{-1})	K_o (dyne/cm^2) * 10^5	K_t (dyne/cm^2) * 10^5	A–O (Å)	B–O (Å)
0.00	240.1	560	461	1.76	3.04	1.8283	2.1111
0.08	244.8	539	464	1.80	2.95	1.8286	2.1115
0.16	249.5	557	454	1.72	2.99	1.8313	2.1147
0.24	253.1	552	460	1.77	3.01	1.8311	2.1144
0.32	259.0	558	452	1.71	2.99	1.8306	2.1138

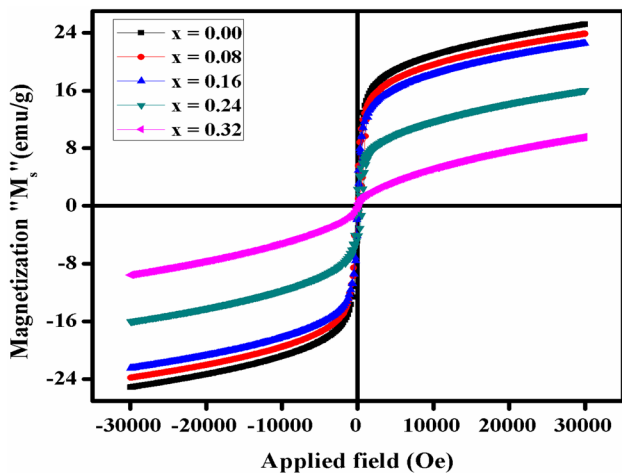


Fig. 7 M–H loops of $\text{Cu}_{0.5}\text{Zn}_{0.5}\text{In}_x\text{Fe}_{2-x}\text{O}_4$ ferrites

appeared around 1638 cm^{-1} attributed to O–H stretching vibrations [48]. The variation in the lattice parameter related to the expansion and contraction of the metal–oxygen bond length of crystallographic sites [49]. The incorporation of indium in copper–zinc ferrites may transfer ferric ions from B sites to A-sites. It is the reason why the vibrational frequency of the B site increases and A-site decreases [50]. The force constant behavior described on the basis of vibrational frequencies. Table 4 reveals the force constant of tetrahedral site followed by the vibrational frequencies of metals oxygen at tetrahedral sites and having the same behavior. The force constant of

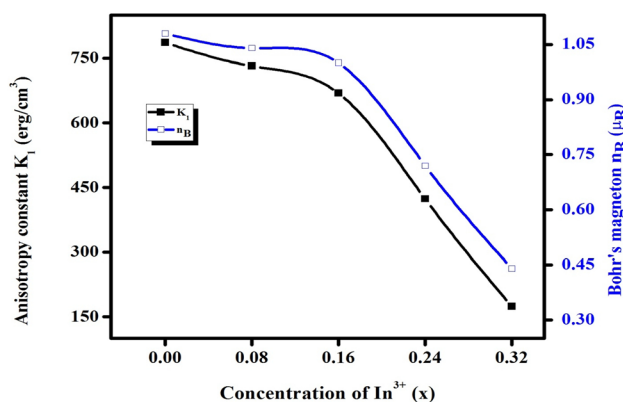
octahedral sites altered with variations of vibrational frequency of metals–oxygen bonds at octahedral sites [51].

3.4 VSM analysis

The magnetic behavior of synthesized ferrites was estimated from M – H loops recorded at room temperature by VSM. The synthesized nano ferrites exhibited narrow hysteresis loops with a small value of coercivity which is evidence for the soft nature of prepared samples. It is clear from Fig. 7 that pure and substituted Cu–Zn ferrites revealed ferromagnetic nature. All the magnetic parameters are determined from hysteresis loops and presented in Table 5. The variations in magnetization as a function of applied field are studied and depicted in Fig. 7. The value of saturation magnetization decreases with the inclusion of indium [52]. The decrease in M_s attributed to the nonmagnetic In^{3+} ions entering into the lattice of copper–zinc ferrites at B sites and reduces the number of Fe^{3+} ions on octahedral sites. It decreases the magnetic moment of octahedral sites. The migration of ferroic ions from tetrahedral sites to octahedral sites increases the magnetic moment of A-sites. As a result net magnetization decreases with the inclusion of non-magnetic ions in the spinel lattice of Cu–Zn nanoferrites. Present results are resembled with the previously reported results [53]. The decrease in M_s

Table 5 The magnetic parameters of Cu–Zn–In–Fe–O system

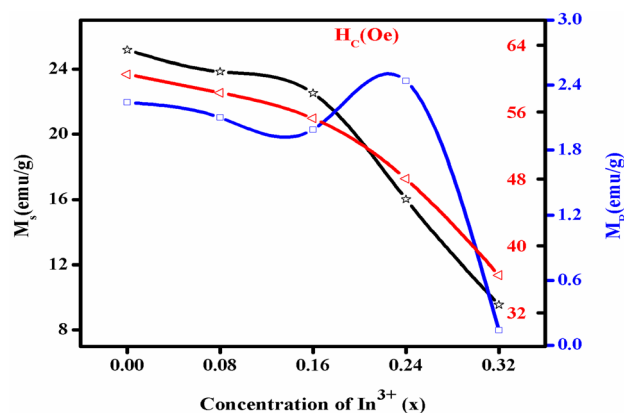
Concentration, x	Saturation magnetization, M_s (emu/g)	Retentivity, M_R (emu/g)	Coercivity, H_c (Oe)	Squareness ratio, R	Anisotropy constant, K_1 (erg/cm ³)	Bohr's magneton, n_B (μ_B)
0.00	25.16	2.19	62.48	0.0872	786.05	1.08
0.08	23.84	2.13	61.41	0.0894	732.06	1.04
0.16	22.52	1.99	59.41	0.0885	669.02	1.00
0.24	16.03	1.12	47.82	0.0513	423.68	0.72
0.32	9.55	0.14	36.19	0.0141	173.89	0.44

**Fig. 8** The variation in anisotropy constant and Bohr's magneton as function of indium concentration

can be described by Neel's two sub lattice model given by: (1)

$$M = M_B - M_A. \quad (1)$$

M_B and M_A are magnetic moments of octahedral and tetrahedral sites, respectively. The magnetic moment is originated due to the spin orientation of two sub lattices which are aligned in an antiparallel direction. The exchange interactions present in the spinel ferrites are A–A, B–B and A–B. In the spinel lattice A–B exchange interaction is predominant than the other two types. If nonmagnetic In³⁺ ions preferred octahedral sites and replaced magnetic ions Fe³⁺ from B site. The magnetic moment of B sites reduces even if the magnetic moment of the A-site remains the same which may cause a decrease in saturation magnetization. This decrease in saturation magnetization may be due to the appearance of secondary phases. When secondary phase appeared it distort the structure and charge carriers are piles up at grain boundaries. Moreover, iron ions are isolated from the lattice which decreases the magnetization.

**Fig. 9** The deviation in M_s , M_R and H_c of In³⁺ substituted copper zinc ferrites

Bohr's magneton decreases due to an increase of In³⁺ content and depicted in Fig. 8. It is another reason for the decrease in M_s [43].

The small value of M_R and H_c indicated the presence of single-domain particles [54]. The variations in M_s , H_c , and M_R are shown in Fig. 9. The decrease in coercivity with the substitution of In³⁺ ions is observed. This decrease is attributed to the effect of magnetocrystalline anisotropy. The indium has zero angular momentum and did not take part in magnetocrystalline anisotropy. When In³⁺ ions were replaced with iron, spin–orbit coupling decreases which reduced the coercivity value [55]. The anisotropy constant is calculated and depicted in Table 5. The anisotropy constant is reduced with the inclusion of In³⁺ ions. This happened due to indium having a smaller value of anisotropy constant than iron. As a result, the value of coercivity was decreased. The decrease in the value of the anisotropy constant was due to decrease in domain wall energy [56]. The squareness ratio estimated from remanence and saturation magnetization. The value of M_R and M_s are

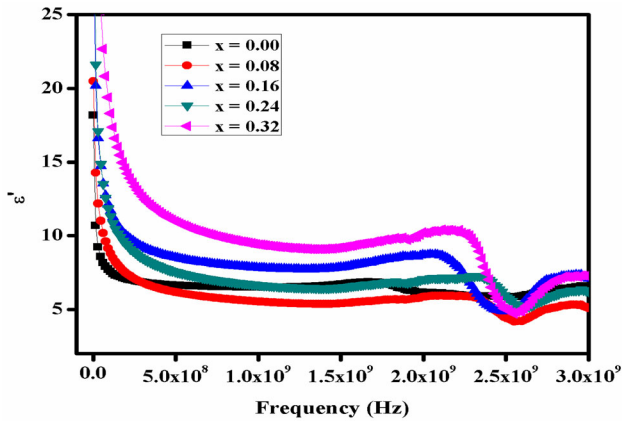


Fig. 10 Dielectric constant versus frequency of indium substituted Cu–Zn ferrites

declined which decreases the squareness ratio. The value of squareness ratio is very small which suggested that indium incorporated copper–zinc ferrites are useful for high-frequency applications [57].

3.5 Dielectric studies

The dielectric constant (ϵ') is used to elucidate the speed of electromagnetic wave travel through the medium. The materials that possessed a high value of ϵ' were used to store charge [58]. The dielectric parameters are recorded in the frequency range of 1 MHz to 3 GHz. Figure 10 shows the frequency-dependent dielectric constant. The ϵ' has a large value at a low frequency while small value at high-frequency which is the general behavior of ferrites materials. Dielectric constant at low frequency decreases rapidly while it reduces slowly at high-frequency and became almost frequency independent. The resonance peaks are observed above 2.5 GHz. The behavior of dielectric constant is associated with space charge polarization [59]. The dielectric constant behavior is ascribed by Maxwell–Wagner model. The polarization phenomenon occurred due to hopping between ferrous and ferric ions. When frequency reaches up to a definite point, the charge carrier cannot follow the variation in the AC applied field. As a result, the dielectric constant exhibited frequency-independent behavior [60].

The relaxation phenomenon that appeared in the dielectric constant directly related to the polarization of substances. The space charge polarization occurred between Fe^{2+} and Fe^{3+} due to hopping phenomenon. According to Koop’s theory, two conducting grains

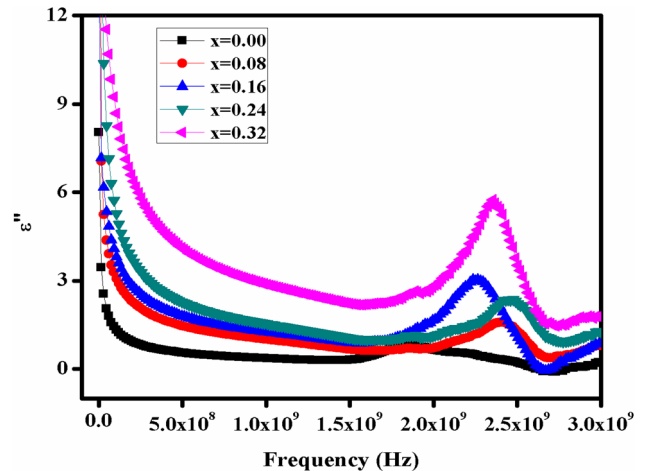


Fig. 11 Dielectric loss as function of frequency of Cu–Zn ferrites

layers are separated by a resistive layer known as grain boundaries [61]. The charges pile up at grain boundaries which mainly contribute to the dielectric constant. The concentration of ferrous ions increased at octahedral sites which may increase space charge polarization. As a result dielectric constant increased. Resonance peaks beyond 2.5 GHz occurred due to the matching of charge carrier’s frequency with the externally applied field frequency. Peaking behavior is observed when the frequency of charge carriers matched with the AC applied field. It increases power loss and resonance peak appeared [62]. The dielectric loss of indium incorporated Cu–Zn nano ferrites is depicted in Fig. 11. It was seen that dielectric loss was found to decrease as the externally applied field increased [63].

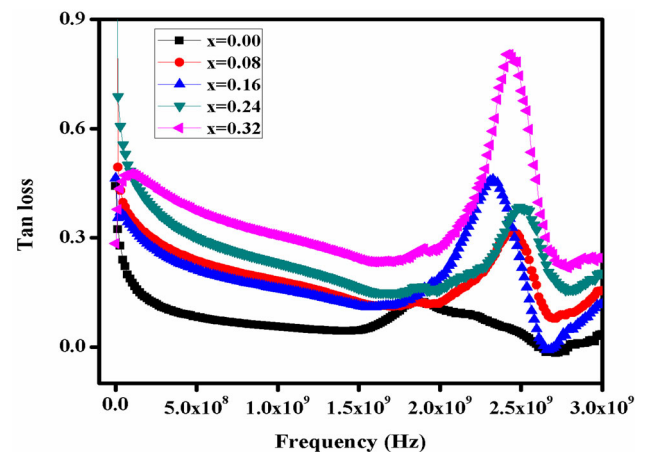


Fig. 12 Frequency dependent tan loss of indium substituted Cu–Zn ferrites

In dielectric material, a dielectric loss estimated the dissipation of energy. The material that possessed high conductivity also has a high dielectric loss and vice versa. The resonance peaks observed in the high-frequency region were explained briefly in the above section. The dielectric loss tangent of indium inclusion copper–zinc ferrites is displayed in Fig. 12. It is the ratio of dielectric loss to dielectric constant. The variation in $\tan\delta$ depends upon various factors such as compositions, annealing temperature, and surface morphology. The value of $\tan\delta$ is reduced with the increase in frequency [64]. The dielectric losses are low at high-frequency due to charge carriers no longer obey the applied field. The resonance phenomenon is observed due to the coinciding of hopping frequency with externally applied field frequency. If the content of In^{3+} is added in a fixed ratio then the conduction mechanism is proportional to concentration of iron ions which is responsible for a decrease in \tan loss. All the results of indium substituted Cu–Zn nano ferrites matched with the reported results and suggested these materials are beneficial for microwave appliances at high-frequency [65]. AC conductivity is calculated by following relation. (2)

$$\sigma_{ac} = \varepsilon_0 \varepsilon' \omega \tan \delta. \quad (2)$$

Deviation in AC conductivity versus frequency shows in Fig. 13. The variation in σ_{ac} was mainly depends upon on frequency. AC conductivity increase with the increase of frequency. The behavior of AC conductivity is described with the help of Koop's theory. The behavior of grains and grain boundaries is different at different frequencies and

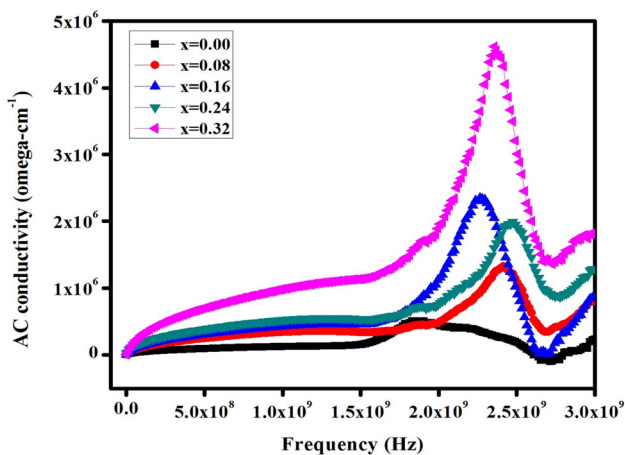


Fig. 13 AC conductivity of In^{3+} incorporated Cu–Zn ferrites

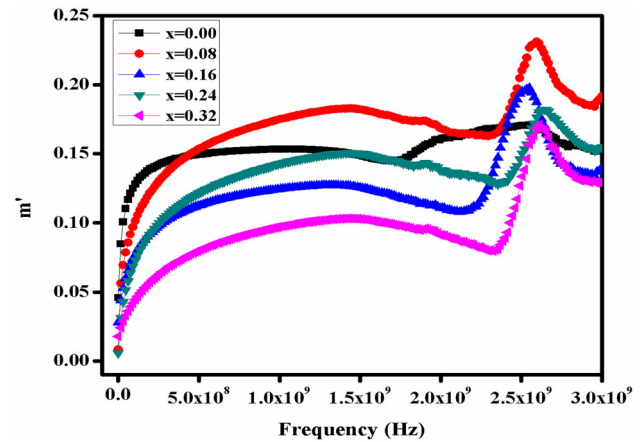


Fig. 14 Frequency dependent M' of In^{3+} incorporated Cu–Zn ferrites

exhibited frequency-dependent behavior. The grain boundaries are active at a low frequency produced obstruction and exhibited a decrease in the mobility of charge carriers. Thus conductivity is small at low frequency [66]. At higher frequency, grains are active that are less resistive than grain boundaries. The conduction mechanism is increased due to a rise in frequency which caused an increase in σ_{ac} . The increasing field frequency increases the hopping frequency between Fe^{2+} and Fe^{3+} ions consequently AC conductivity increased. The resonance peak is observed in AC conductivity attributed to the homogenous structure of prepared ferrites material. The rapid decrease in Ac conductivity is due to lag behind phenomenon of charges and applied field [67].

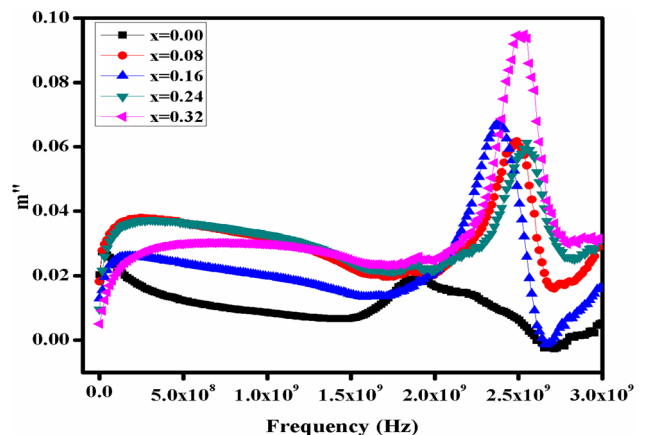


Fig. 15 M'' versus frequency of indium substituted copper–zinc ferrites

The variation in M' versus frequency is displayed in Fig. 14. The difference in grains and grain boundaries contribution is analyzed from the electric modulus [68]. It also gives information about the conduction and relaxation process. The value of M' is directly proportional to frequency. After a certain frequency, its value approaches the maximum and becomes almost constant. This phenomenon is caused due to the conduction process of electrons of long-range mobility. The short-range mobility of charge carriers is responsible for saturating the value of M' into an asymptotic single value. This happened

due to a decrease in hopping length at B sites [69, 70]. Figure 15 reveals the frequency-dependent imaginary part of modulus. It decreases with the increase of frequency while the resonance peak is observed at higher frequencies. The value of resonance peak increases with the increase of indium content. The region below the maximum value of M'' due to long-range mobility of charge carriers while above this value charge carriers were restricted to a shorter distance and confined into the potential well [71].

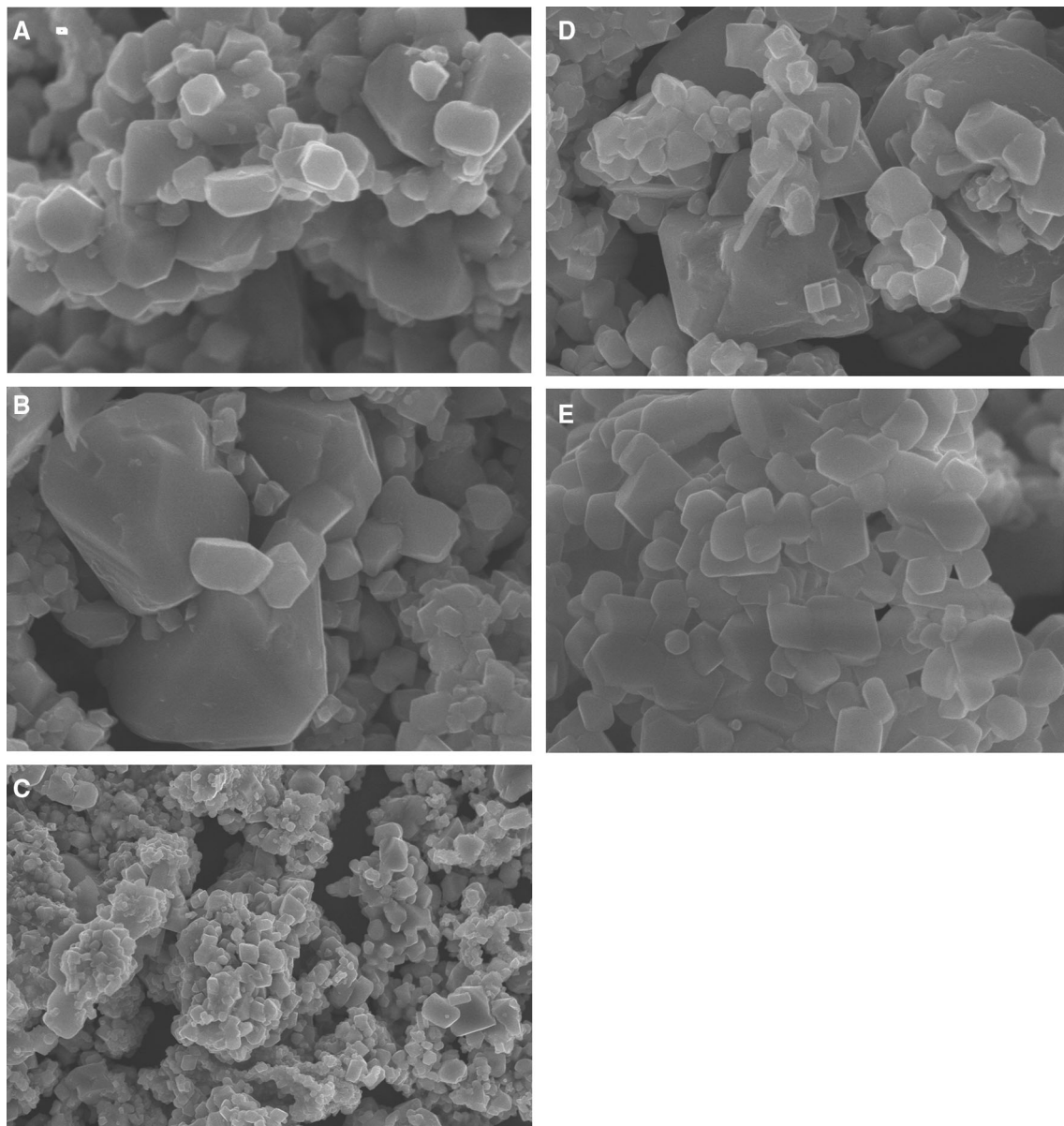


Fig. 16 SEM images of In^{3+} included Cu-Zn ferrites

3.6 SEM analysis

The morphology of prepared ferrites is analyzed by SEM (scanning electron microscopy) and images are shown in Fig. 16. The micrograph exhibited agglomeration of grain structure. The agglomeration in these ferrites is due to magnetic interaction between the particles. It is observed from SEM micrograph that grain size decreases with the substitution of indium in Cu–Zn ferrites. All the samples revealed crack free and regular structure. The variation in grain size indicated the fabrication of indium substituted copper–zinc ferrites [72–74].

4 Conclusions

Indium (In^{3+}) incorporated Cu–Zn magnetic oxides were synthesized via sol–gel auto-combustion technique. The structural analysis revealed the cubic spinel structure of all samples. Initially, the lattice constant increased for $x \leq 0.16$ and reduced thereafter. The value of crystallite size was monotonically decreased and found in the range of 9.37–14.76 nm. X-ray density increased from 5.30 to 5.69 and bulk density remained in the range of 2.66 to 3.06 g/cm^3 . Strain and dislocation densities were increased (0.113–0.179 and 0.013–0.033) with the incorporation of In^{3+} ions in Cu–Zn magnetic oxides. Force constants and band position variation confirmed the substitution of indium in these materials. Various concentrations of In^{3+} ions greatly affected the values of magnetic parameters. The value of M_s , M_R , and H_c was decreased with the increase of dopant concentration. The magnetic analysis revealed that the value of squareness ratio and anisotropy constant decreased with In^{3+} content. The dielectric parameters were found to increase as indium contents were increased. The value of Bohr's magnetron also decreased from 1.08 to 0.44 μ_B . The small value of squareness ratio and anisotropy constant with moderate saturation magnetization may suggest that prepared materials may have potential in switching and high-frequency applications (Figs. 14, 15, 16).

Acknowledgements

The author extends their appreciation to the Researchers Supporting Project Number (RSP-2021/

394), King Saud University, Riyadh, Saudi Arabia. The authors extend their sincere appreciation to the Deanship of Scientific Research at Princess Nourah bint Abdulrahman University through the Fast-Track Research Funding Program.

References

1. L.-A. Han et al., Critical behavior in $\text{Ni}_{0.15}\text{Cu}_{0.15}\text{Zn}_{0.7}\text{Fe}_2\text{O}_4$ spinel ferrite. *Ceram. Int.* **45**(11), 14322–14326 (2019)
2. J. Hu et al., Characterization of texture and magnetic properties of $\text{Ni}_{0.5}\text{Zn}_{0.5}\text{Ti}_x\text{Fe}_{2-x}\text{O}_4$ spinel ferrites. *J. Magn. Magn. Mater.* **489**, 165411 (2019)
3. N. Hamdaoui et al., Cd-doping effect on morphologic, structural, magnetic and electrical properties of $\text{Ni}_{0.6-x}\text{Cd}_x\text{Mg}_{0.4}\text{Fe}_2\text{O}_4$ spinel ferrite ($0 \leq x \leq 0.4$). *J. Alloys Compds* **803**, 964–970 (2019)
4. D. Jnaneshwara et al., Role of Cu^{2+} ions substitution in magnetic and conductivity behavior of nano- CoFe_2O_4 . *Spectrochim. Acta A* **132**, 256–262 (2014)
5. M. Houshiar, L. Jamilpanah, Effect of Cu dopant on the structural, magnetic and electrical properties of Ni–Zn ferrites. *Mater. Res. Bull.* **98**, 213–218 (2018)
6. R.A. Jasso-Terán et al., Synthesis, characterization and hemolysis studies of $\text{Zn}_{(1-x)}\text{Ca}_x\text{Fe}_2\text{O}_4$ ferrites synthesized by sol–gel for hyperthermia treatment applications. *J. Magn. Magn. Mater.* **427**, 241–244 (2017)
7. X. Wu et al., Influence of particle size on the magnetic spectrum of NiCuZn ferrites for electromagnetic shielding applications. *J. Magn. Magn. Mater.* **401**, 1093–1096 (2016)
8. W.-S. Chen et al., Effects of titanate coupling agent on the dielectric properties of NiZn ferrite powders–epoxy resin coatings. *Ceram. Int.* **37**(7), 2347–2352 (2011)
9. M.N. Akhtar et al., Evaluation of structural, morphological and magnetic properties of CuZnNi ($\text{Cu}_x\text{Zn}_{0.5-x}\text{Ni}_{0.5}\text{Fe}_2\text{O}_4$) nanocrystalline ferrites for core, switching and MLCI's applications. *J. Magn. Magn. Mater.* **421**, 260–268 (2017)
10. S. Akhter et al., Glassy behavior of diluted Cu–Zn ferrites. *J. Magn. Magn. Mater.* **452**, 261–265 (2018)
11. M. Junaid et al., Impact of indium substitution on dielectric and magnetic properties of $\text{Cu}_{0.5}\text{Ni}_{0.5}\text{Fe}_{2-x}\text{O}_4$ ferrite materials. *Ceram. Int.* **45**(10), 13431–13437 (2019)
12. A. Raghavender, S.E. Shirsath, K.V. Kumar, Synthesis and study of nanocrystalline Ni–Cu–Zn ferrites prepared by oxalate based precursor method. *J. Alloys Compds* **509**(25), 7004–7008 (2011)
13. S. Mahmud et al., Influence of microstructure on the complex permeability of spinel type Ni–Zn ferrite. *J. Magn. Magn. Mater.* **305**(1), 269–274 (2006)

14. S.E. Shirsath et al., Enhanced magnetic properties of Dy³⁺ substituted Ni–Cu–Zn ferrite nanoparticles. *Appl. Phys. Lett.* **100**(4), 042407 (2012)
15. M. Hashim et al., Influence of Cr³⁺ ion on the structural, AC conductivity and magnetic properties of nanocrystalline Ni–Mg ferrite. *Ceram. Int.* **39**(2), 1807–1819 (2013)
16. S. Akhter et al., Magnetic and magnetocaloric properties of Cu_{1-x}Zn_xFe₂O₄ (x = 0.6, 0.7, 0.8) ferrites. *J. Magn. Magn. Mater.* **367**, 75–80 (2014)
17. S. Amor et al., Modulation of magnetism and study of impedance and alternating current conductivity of Zn_{0.4}Ni_{0.6}Fe₂O₄ spinel ferrite. *J. Mol. Struct.* **1184**, 298–304 (2019)
18. M.M. Abutalib, A. Rajeh, Influence of MWCNTs/Li-doped TiO₂ nanoparticles on the structural, thermal, electrical and mechanical properties of poly (ethylene oxide)/poly (methylmethacrylate) composite. *J. Organomet. Chem.* **918**, 121309 (2020)
19. M.M. Abutalib, A. Rajeh, Preparation and characterization of polyaniline/sodium alginate-doped TiO₂ nanoparticles with promising mechanical and electrical properties and antimicrobial activity for food packaging applications. *J. Mater. Sci. Mater. Electron.* **31**(12), 9430–9442 (2020)
20. A.M. Hezma, A. Rajeh, M.A. Mannaa, An insight into the effect of zinc oxide nanoparticles on the structural, thermal, mechanical properties and antimicrobial activity of Cs/PVA composite. *Colloids Surf. A* **581**, 123821 (2019)
21. S. Ata-Allah, M. Yehia, Transport properties and conduction mechanisms in CuFe₂O₄ and Cu_{1-x}Zn_xGa_{0.3}Fe_{1.7}O₄ compounds. *Physica B* **404**(16), 2382–2388 (2009)
22. B. Cruz-Franco et al., Magnetic properties of nanostructured spinel ferrites. *IEEE Trans. Magn.* **50**(4), 1–6 (2014)
23. S. Yunus et al., Neutron diffraction studies of the diluted spinel ferrite Zn_xMg_{0.75-x}Cu_{0.25}Fe₂O₄. *J. Magn. Magn. Mater.* **232**(3), 121–132 (2001)
24. X. Zhu et al., A comparative study of spinel ZnFe₂O₄ ferrites obtained via a hydrothermal and a ceramic route: structural and magnetic properties. *Ceram. Int.* **47**(11), 15173–15179 (2021)
25. T. Ajeesha et al., Nickel substituted MgFe₂O₄ nanoparticles via co-precipitation method for photocatalytic applications. *Physica B* **606**, 412660 (2021)
26. Yunasfi et al., Synthesis of NiCe_xFe_(2-x)O₄ (0 ≤ x ≤ 0.05) as microwave absorbing materials via solid-state reaction method. *J. Magn. Magn. Mater.* **532**, 167985 (2021)
27. M. Junaid et al., Structural, spectral, dielectric and magnetic properties of Tb–Dy doped Li–Ni nano-ferrites synthesized via micro-emulsion route. *J. Magn. Magn. Mater.* **419**, 338–344 (2016)
28. J. Xie et al., Microwave-absorbing properties of NiCoZn spinel ferrites. *J. Magn. Magn. Mater.* **314**(1), 37–42 (2007)
29. S.E. Shirsath et al., Frequency, temperature and In³⁺ dependent electrical conduction in NiFe₂O₄ powder. *Powder Technol.* **212**(1), 218–223 (2011)
30. M. Hashim et al., High temperature dielectric studies of indium-substituted NiCuZn nanoferrites. *J. Phys. Chem. Solids* **112**, 29–36 (2018)
31. C.C. Naik, A.V. Salker, Investigation of the effect of fractional In³⁺ ion substitution on the structural, magnetic, and dielectric properties of Co–Cu ferrite. *J. Phys. Chem. Solids* **133**, 151–162 (2019)
32. A.V. Humbe et al., Impact of Jahn Teller ion on magnetic and semiconducting behaviour of Ni–Zn spinel ferrite synthesized by nitrate–citrate route. *J. Alloys Compds* **691**, 343–354 (2017)
33. L.-Z. Li et al., Structural and magnetic properties of strontium substituted NiZn ferrite nanopowders. *Ceram. Int.* **42**(11), 13238–13241 (2016)
34. M.P. Reddy et al., Influence of copper substitution on magnetic and electrical properties of MgCuZn ferrite prepared by microwave sintering method. *Mater. Sci. Eng. C* **30**(8), 1094–1099 (2010)
35. S.L. Reddy et al., Synthesis and spectroscopic characterization of copper zinc aluminum nanoferrite particles. *Spectrochim. Acta A* **127**, 361–369 (2014)
36. R. Sharma et al., Improvement in magnetic behaviour of cobalt doped magnesium zinc nano-ferrites via co-precipitation route. *J. Alloys Compds* **684**, 569–581 (2016)
37. M.D. Hossain et al., Frequency and temperature dependent magnetic properties with structural Rietveld refinement of Co_{0.25}Zn_{0.75}Y_xFe_{2-x}O₄ ferrites. *J. Magn. Magn. Mater.* **493**, 165696 (2020)
38. G. Lal et al., Rietveld refinement, Raman, optical, dielectric, Mössbauer and magnetic characterization of superparamagnetic fcc-CaFe₂O₄ nanoparticles. *Ceram. Int.* **45**(5), 5837–5847 (2019)
39. K. Sun et al., Rietveld refinement, microstructure and ferromagnetic resonance linewidth of iron-deficiency NiCuZn ferrites. *J. Alloys Compds* **681**, 139–145 (2016)
40. A.V. Humbe et al., Rietveld refinement, morphology and superparamagnetism of nanocrystalline Ni_{0.70-x}Cu_xZn_{0.30}Fe₂O₄ spinel ferrite. *Ceram. Int.* **44**(5), 5466–5472 (2018)
41. M.N. Akhtar et al., Impact of Co doping on physical, structural, microstructural and magnetic features of MgZn nanoferrites for high frequency applications. *Ceram. Int.* **46**(2), 1750–1759 (2020)
42. M.D. Rahaman et al., Investigation of structural, morphological and electromagnetic properties of

- Mg_{0.25}Mn_{0.25}Zn_{0.5-x}Sr_xFe₂O₄ ferrites. *J. Magn. Magn. Mater.* **451**, 391–406 (2018)
43. S. Mansour, M. Abdo, F. Kzar, Effect of Cr dopant on the structural, magnetic and dielectric properties of Cu–Zn nanoferrites. *J. Magn. Magn. Mater.* **465**, 176–185 (2018)
 44. M. Sharif et al., Impact of Co and Mn substitution on structural and dielectric properties of lithium soft ferrites. *Physica B* **567**, 45–50 (2019)
 45. M. Sundararajan et al., Microwave combustion synthesis of Co_{1-x}Zn_xFe₂O₄ (0 ≤ x ≤ 0.5): structural, magnetic, optical and vibrational spectroscopic studies. *Spectrochim. Acta A* **140**, 421–430 (2015)
 46. M. Arshad et al., Structural and magnetic properties variation of manganese ferrites via Co–Ni substitution. *J. Magn. Magn. Mater.* **474**, 98–103 (2019)
 47. R.S. Yadav et al., Structural, magnetic, elastic, dielectric and electrical properties of hot-press sintered Co_{1-x}Zn_xFe₂O₄ (x = 0.0, 0.5) spinel ferrite nanoparticles. *J. Magn. Magn. Mater.* **447**, 48–57 (2018)
 48. S. Debnath et al., X-ray diffraction analysis for the determination of elastic properties of zinc-doped manganese spinel ferrite nanocrystals (Mn_{0.75}Zn_{0.25}Fe₂O₄), along with the determination of ionic radii, bond lengths, and hopping lengths. *J. Phys. Chem. Solids* **134**, 105–114 (2019)
 49. A. Gholizadeh, A comparative study of the physical properties of Cu–Zn ferrites annealed under different atmospheres and temperatures: magnetic enhancement of Cu_{0.5}Zn_{0.5}Fe₂O₄ nanoparticles by a reducing atmosphere. *J. Magn. Magn. Mater.* **452**, 389–397 (2018)
 50. M. Deepty et al., XRD, EDX, FTIR and ESR spectroscopic studies of co-precipitated Mn-substituted Zn–ferrite nanoparticles. *Ceram. Int.* **45**(6), 8037–8044 (2019)
 51. T.P. Poudel et al., The effect of gadolinium substitution in inverse spinel nickel ferrite: structural, magnetic, and Mössbauer study. *J. Alloys Compds* **802**, 609–619 (2019)
 52. K. Jalaiah et al., Co-dopant affect on the structural, electrical and magnetic properties of zirconium and copper co-substituted Ni_{0.75}Zn_{0.25}Fe₂O₄ spinel ferrites synthesized by sol–gel method. *Chin. J. Phys.* **56**(5), 2039–2051 (2018)
 53. A.C. Lima et al., The effect of Sr²⁺ on the structure and magnetic properties of nanocrystalline cobalt ferrite. *Mater. Lett.* **145**, 56–58 (2015)
 54. M. Abdullah Dar et al., Study of structure and magnetic properties of Ni–Zn ferrite nano-particles synthesized via co-precipitation and reverse micro-emulsion technique. *Appl. Nanosci.* **4**(6), 675–682 (2014)
 55. I. Maghsoudi et al., Synthesis and characterization of NiAl_xFe_{2-x}O₄ magnetic spinel ferrites produced by conventional method. *Powder Technol.* **235**, 110–114 (2013)
 56. S.E. Shirsath et al., Self-ignited high temperature synthesis and enhanced super-exchange interactions of Ho³⁺–Mn²⁺–Fe³⁺–O²⁻ ferromagnetic nanoparticles. *Phys. Chem. Chem. Phys.* **16**(6), 2347–2357 (2014)
 57. N.-N. Jiang et al., Influence of zinc concentration on structure, complex permittivity and permeability of Ni–Zn ferrites at high frequency. *J. Magn. Magn. Mater.* **401**, 370–377 (2016)
 58. M. Dilshad et al., Fabrication and characterization of Ni_{1+x}Zr_xFe_{2-2x}O₄ nanoparticles for potential applications in high frequency devices. *Ceram. Int.* **42**(14), 16359–16363 (2016)
 59. M. Ejaz et al., Influence of Yb³⁺ on the structural, dielectric and magnetic properties of Mg_{0.7}Co_{0.3}Fe₂O₄ nanocrystallites synthesized via co-precipitation route. *J. Magn. Magn. Mater.* **404**, 257–264 (2016)
 60. M. Asif Iqbal et al., High frequency dielectric properties of Eu³⁺-substituted Li–Mg ferrites synthesized by sol–gel auto-combustion method. *J. Alloys Compds* **586**, 404–410 (2014)
 61. P. Choudhary, D. Varshney, Dielectric relaxation behavior and impedance studies of Cu²⁺ ion doped Mg–Zn spinel nanoferrites. *Solid State Commun.* **271**, 89–96 (2018)
 62. M. Anis-ur-Rehman, G. Asghar, Variation in structural and dielectric properties of co-precipitated nanoparticles strontium ferrites due to value of pH. *J. Alloys Compds* **509**(2), 435–439 (2011)
 63. I. Gul, A. Maqsood, Structural, magnetic and electrical properties of cobalt ferrites prepared by the sol–gel route. *J. Alloys Compds* **465**(1–2), 227–231 (2008)
 64. Z.A. Gilani et al., Structural and electromagnetic behavior evaluation of Nd-doped lithium–cobalt nanocrystals for recording media applications. *J. Alloys Compds* **639**, 268–273 (2015)
 65. V. Manikandan et al., Structural, dielectric and enhanced soft magnetic properties of lithium (Li) substituted nickel ferrite (NiFe₂O₄) nanoparticles. *J. Magn. Magn. Mater.* **465**, 634–639 (2018)
 66. A.S. Fawzi, A. Sheikh, V. Mathe, Structural, dielectric properties and AC conductivity of Ni_(1-x)Zn_xFe₂O₄ spinel ferrites. *J. Alloys Compds* **502**(1), 231–237 (2010)
 67. M. Elkestawy, AC conductivity and dielectric properties of Zn_{1-x}Cu_xCr_{0.8}Fe₁₂O₄ spinel ferrites. *J. Alloys Compds* **492**(1–2), 616–620 (2010)
 68. N. Hamdaoui et al., Structural, magnetic and dielectric properties of Ni_{0.6}Mg_{0.4}Fe₂O₄ ferromagnetic ferrite prepared by sol gel method. *Ceram. Int.* **45**(13), 16458–16465 (2019)
 69. E. AlArfaj et al., Effects of Co substitution on the microstructural, infrared, and electrical properties of Mg_{0.6-x}Co_xZn_{0.4}Fe₂O₄ ferrites. *J. Supercond. Nov. Magn.* **31**(12), 4107–4116 (2018)

70. N. Vasoya et al., Electric modulus, scaling and modeling of dielectric properties for Mn^{2+} - Si^{4+} co-substituted Mn–Zn ferrites. *J. Electron. Mater.* **45**(2), 917–927 (2016)
71. J. Joshi et al., Dielectric relaxation, complex impedance and modulus spectroscopic studies of mix phase rod like cobalt sulfide nanoparticles. *Mater. Res. Bull.* **93**, 63–73 (2017)
72. Q. Khan et al., Structural features and dielectric behavior of Al substituted $\text{Cu}_{0.7}\text{Ni}_{0.3}\text{Fe}_2\text{O}_4$ ferrites. *Mater. Chem. Phys.* **273**, 125028 (2021)
73. M.P. Dojcinovic et al., Mixed Mg–Co spinel ferrites: structure, morphology, magnetic and photocatalytic properties. *J. Alloys Compds* **855**, 157429 (2021)
74. M. Junaid et al., Structural, spectral, dielectric and magnetic properties of indium substituted copper spinel ferrites synthesized via sol gel technique. *Ceram. Int.* **46**(17), 27410–27418 (2020)

Publisher's Note Springer Nature remains neutral with regard to jurisdictional claims in published maps and institutional affiliations.